

Orbital evolution of colliding star and pulsar winds in 2D and 3D: dimensionality, resolution, and grid size effects

V. Bosch-Ramon¹, M.V. Barkov² and M. Perucho³

¹ Departament d'Astronomia i Meteorologia, Institut de Ciències del Cosmos (ICC), Universitat de Barcelona (IEEC-UB), Martí i Franquès 1, 08028 Barcelona, Catalonia, Spain

² Astrophysical Big Bang Laboratory, RIKEN, 2-1 Hirosawa, Wako, Saitama 351-0198, Japan

³ Dept. d'Astronomia i Astrofísica, Universitat de València, C/ Dr. Moliner 50, 46100, Burjassot (València), Spain

Received [date] / Accepted [date]

ABSTRACT

Context. The structure formed by the shocked winds of a massive star and a non-accreting pulsar in a binary system suffers periodic and random variations of orbital and non-linear dynamical origin. The characterization of the evolution of the two-wind interaction region is necessary to understand the non-thermal emission from radio to gamma rays.

Aims. For the first time, we simulate in 3 dimensions the interaction of isotropic stellar and relativistic pulsar winds along one full orbit, on scales well beyond the binary size. We also investigate the impact of grid resolution and size.

Methods. We carry out, with the code *PLUTO*, relativistic hydrodynamical simulations in 2 and 3 dimensions of the interaction of a slow dense wind and a mildly relativistic wind along one full orbit, up to ~ 100 times the binary size. The 2-dimensional simulations are carried out with equal and larger grid resolution and size than in 3 dimensions.

Results. The simulations in 3 dimensions confirm previous results in 2 dimensions, showing a strong shock induced by Coriolis forces that terminates the pulsar wind in all directions, strong bending of the interaction structure against the pulsar motion, and the generation of turbulence. The shocked flows are also subject to a faster development of instabilities in 3 dimensions, which enhances the presence of shocks, two-wind mixing, and the disruption of the interaction structure on large scales. In 2 dimensions, higher resolution simulations confirm lower resolution results, and simulations with larger grid sizes strengthen the case for the loss of global coherence of the interaction structure.

Conclusions. Simulations in 3 dimensions confirm that the interaction of stellar and pulsar winds yields structures that evolve non-linearly and get strongly entangled. The evolution is accompanied by strong kinetic energy dissipation, rapid changes in flow orientation and speed, and turbulent motion. The loss of global coherence is strongly enhanced in 3 dimensions and as the resolution increases.

Key words. Hydrodynamics – X-rays: binaries – Stars: winds, outflows – Radiation mechanisms: nonthermal – Gamma rays: stars

1. Introduction

As already proposed long ago, binary systems hosting a massive star and a powerful non-accreting pulsar can produce gamma rays through the interaction of the stellar and the pulsar winds (e.g. Maraschi & Treves 1981). An actual instance of this kind of object is the binary system PSR B1259–63/(LS2883), which consists of a late O star with a decretion disc (Negueruela et al. 2011) and a 47 ms pulsar (Johnston et al. 1992), and is a powerful GeV and TeV emitter (e.g. Aharonian et al. 2005; Abdo et al. 2011; Tam et al. 2011). Other binaries emitting gamma rays may also pertain to this class, like LS 5039, LS I +61 303, HESS J0632+057 and 1FGL J1018.6–5856 (see, e.g., Barkov & Khangulyan 2012; Paredes et al. 2013; Dubus 2013, and references therein), although the true nature of the compact object in these sources is still unknown. In the whole Galaxy, taking a lifetime for the non-accreting pulsar of a few times 10^5 yr (the age of PSR B1259–63), and the birth rates for high-mass binaries hosting a neutron star (e.g. Portegies Zwart & Yungelson 1999), one might ex-

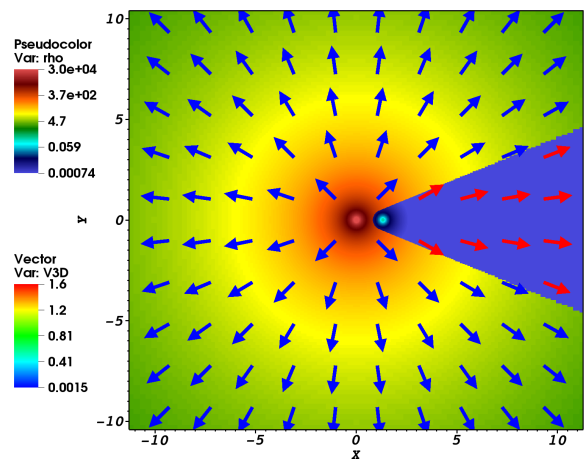


Fig. 1. Density distribution by colour, and arrows representing the flow motion direction, in the orbital plane (XY) for 3Df at the beginning of the simulation ($t = 0$; apastron).

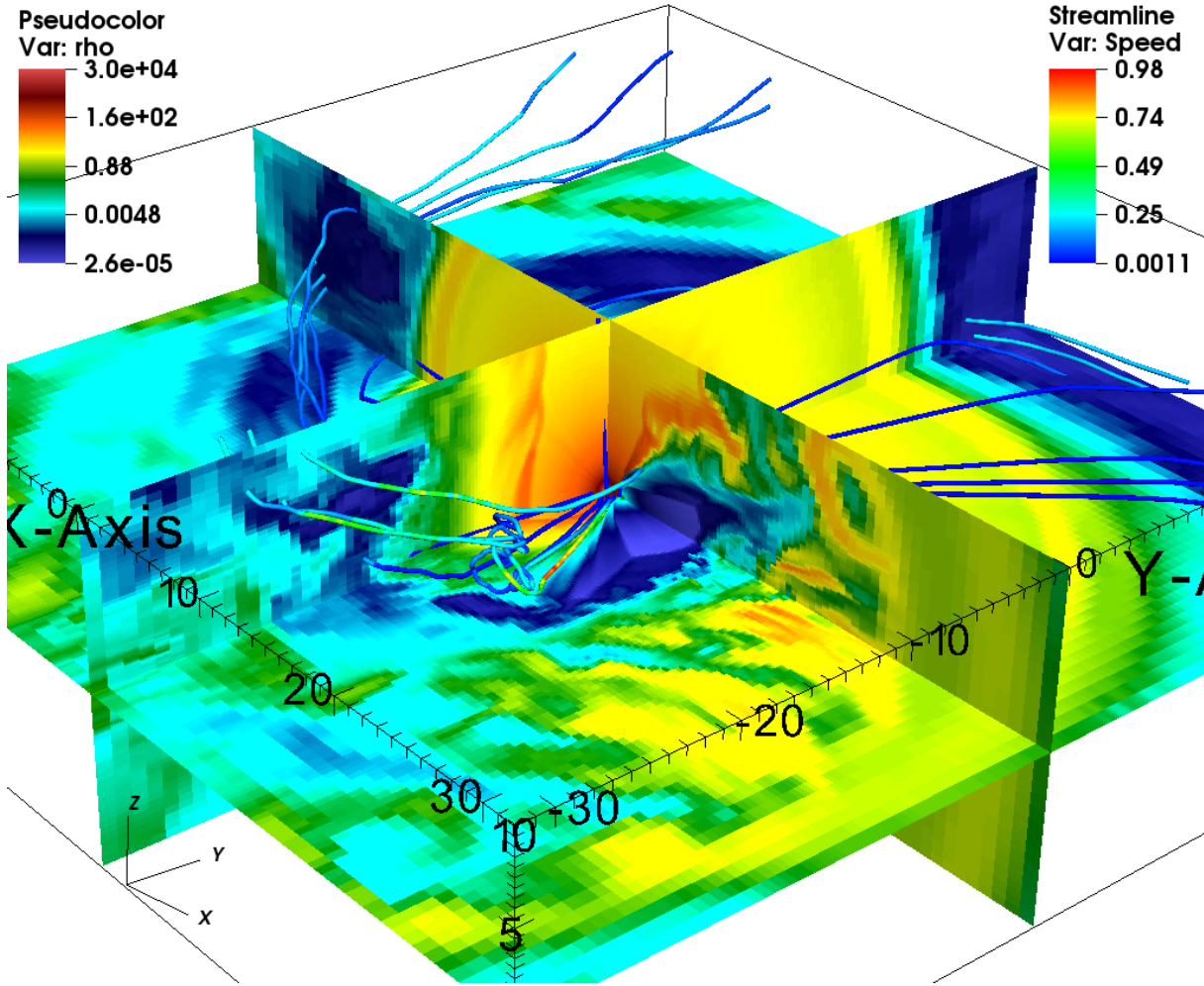


Fig. 2. Representation of the distribution of density in the XY -, XZ - and YZ -planes for 3Dlf at $t = 3.9$ days (apastron). Streamlines are shown in 3D.

pect ~ 100 of these systems (see also Paredes et al. 2013; Dubus 2013).

The rich phenomenology of PSR B1259–63/LS288 (see Chernyakova et al. 2014, for a multi-wavelength study of the 2010 periastron passage), and (possibly) also that of other gamma-ray binaries, is a clear example of the complex processes taking place in the colliding wind region. Given this complexity, there are a number of works devoted to the numerical study of the wind collision region, and its evolution along the orbit and on scales beyond those of the binary (Romero et al. 2007; Bogovalov et al. 2008, 2012; Okazaki et al. 2011; Takata et al. 2012; Bosch-Ramon et al. 2012; Bogovalov et al. 2012; Lamberts et al. 2012b,a, 2013; Paredes-Fortuny et al. 2014). In particular, in Bosch-Ramon et al. (2012) the authors performed 2-dimensional (2D) simulations in planar coordinates of the interaction of a dense, non-relativistic stellar wind and a powerful, mildly relativistic pulsar wind along one full orbit, up to scales ≈ 40 times the orbital separation distance (or orbit semi-major axis a). These simulations showed the early stages of the spiral structure also found in non-relativistic simulations (Lamberts et al. 2012b), but fast growth of instabilities (see also Lamberts et al. 2013) and strong two-wind mixing suggested the eventual disruption of the spiral,

and the isotropization of the mass, momentum and energy fluxes (as predicted in Bosch-Ramon & Barkov 2011).

If the results from Bosch-Ramon et al. (2012) were confirmed, it would imply several important facts: the two-wind interaction process is subject to strongly non-linear processes already within the binary system, the isotropization of the interaction region leads to loss of coherence on scales not far beyond a , eventually becoming a more or less irregular isotropic flow, formed by mixed stellar and pulsar wind, and terminating with a shock on the external medium (interstellar medium or supernova remnant ejecta; see Bosch-Ramon & Barkov 2011). All these dynamical processes would imply the existence of many potential sites for particle acceleration, as shocks, turbulence, shear flows, and non-thermal emission, mainly synchrotron and inverse Compton, from deep inside the system to pc scales.

In this work, we go a step forward in the study of the interaction of the stellar and the pulsar winds including orbital motion. We perform, for the first time, 3-dimensional (3D), relativistic simulations using similar parameters to those adopted in Bosch-Ramon et al. (2012) up to a distance $\sim 30 a$ from the binary. The results obtained in 3D are compared with results found in new 2D simulations in planar coordinates under the same conditions, in particular the number of cells per dimension and grid size. Additional

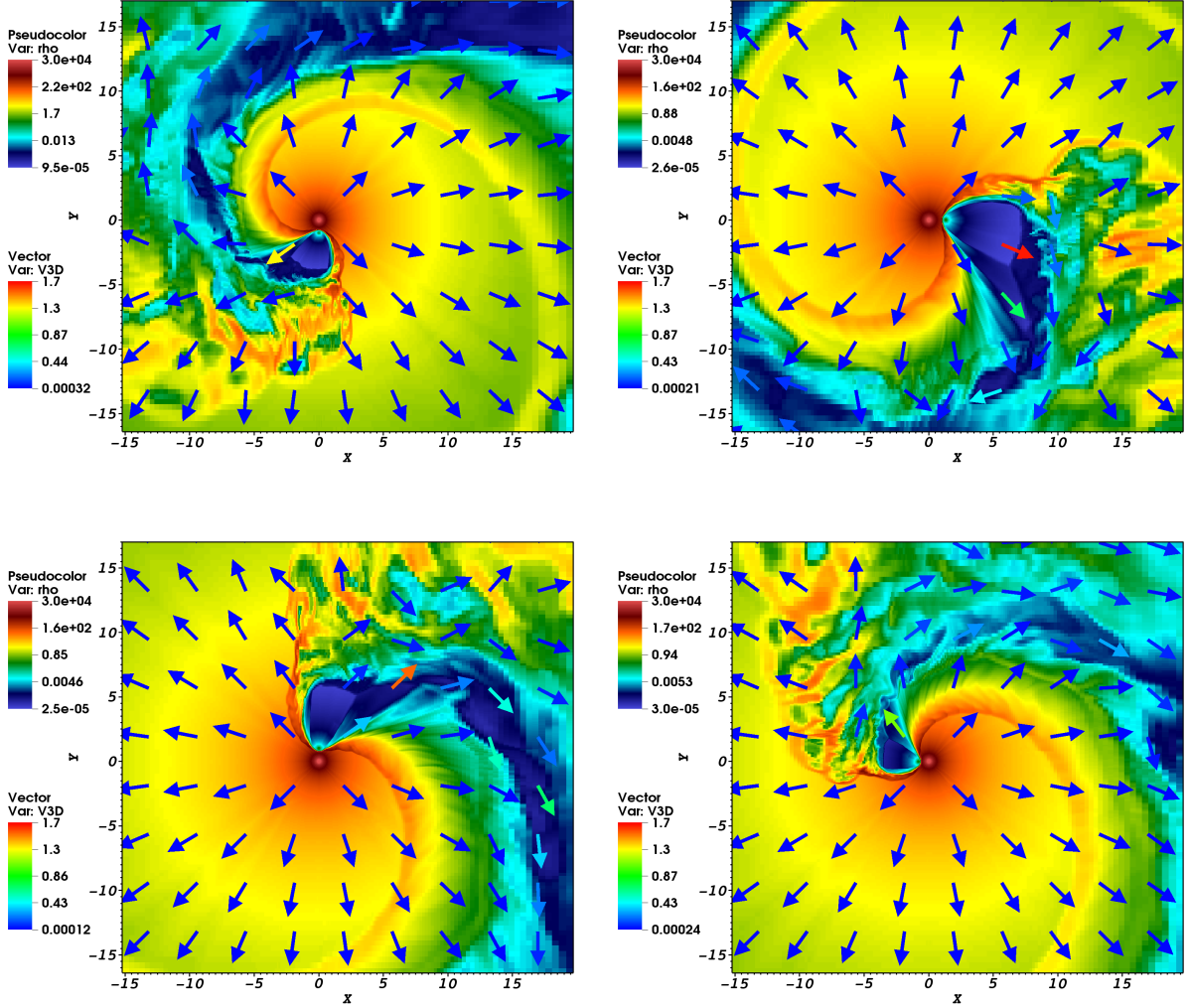


Fig. 3. Density distribution by colour, and arrows representing the flow motion direction, in the orbital plane (XY) for 3Df at: $t = 2.6, 3.9$ (apastron), $5.2, 5.85$ days (periastron) (from top to bottom, and left to right).

2D simulations are also carried out to study the effects of a higher resolution, and a larger grid size up to $\sim 100 a$ from the binary, not reached so far in relativistic simulations.

2. Numerical simulations

The simulations were implemented in 3D and 2D with the *PLUTO* code¹ (Mignone et al. 2007), the piece-parabolic method (PPM) (Colella & Woodward 1984), and an HLLC Riemann Solver (Mignone & Bodo 2005). *PLUTO* is a modular Godunov-type code entirely written in C intended mainly for astrophysical applications and high Mach number flows in multiple spatial dimensions. For this work, it was run through the MPI library in the CFCA cluster of the National Astronomical Observatory of Japan.

The simulated flows were approximated as an ideal, relativistic adiabatic gas with no magnetic field, one particle species, and polytropic index of $4/3$. This index has been fixed at this stage to reduce the time cost of the simulations carried out. A more complete treatment of the

adiabatic index would lead to changes in the Rankine-Hugoniot conditions, in particular for the stellar wind, which actually would also need including thermal cooling (see Sect. 4); at this stage this more complete treatment is left for future work. We adopted a changing resolution in the 3D simulation (model 3Df; see Table 1) to reach larger scales. The computational domain size is $x \in [-32 a, 32 a]$, $y \in [-32 a, 32 a]$, and $z \in [-10 a, 10 a]$. The 3D domain has a resolution of $512 \times 512 \times 256$ cells. The central part of this domain, $x \in [-2 a, 2 a]$, $y \in [-2 a, 2 a]$, and $z \in [-a, a]$, has a resolution of $256 \times 256 \times 128$ cells, and outside this domain the cell size grows exponentially² with distance outwards in each direction. The equivalent uniform resolution for the whole domain would be $4096 \times 4096 \times 2560$ cells. We remark that the adopted resolution came from a compromise between computational costs and a maximal Lorentz factor. The 3D simulations required about 3×10^5 cpu h on NAOJ cluster XC30. To achieve a Lorentz factor ≈ 10 we should have doubled the grid resolution (see Sect. 3.1 in Bosch-Ramon et al. 2012), leading to a computation 16 times longer. Adaptive Mesh Refinement (AMR) was not

¹ Link <http://plutocode.ph.unito.it/index.html>

² Link <http://plutocode.ph.unito.it/files/userguide.pdf>

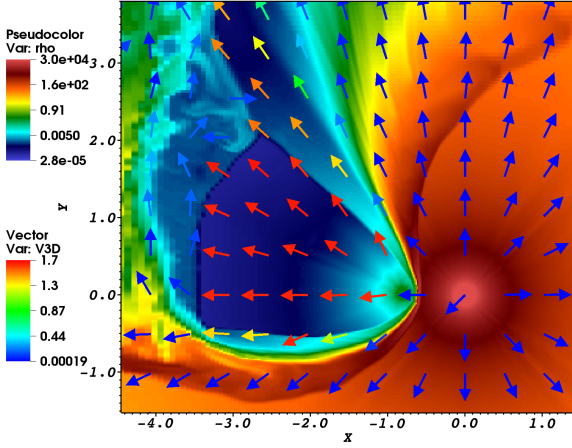


Fig. 4. Zoom in of the region around the pulsar region at periastron shown in Fig. 3.

implemented for these simulations, as in such a kind of problem with strongly turbulent flows the AMR technique fills almost all the computational volume with the smallest scale grid due to growth of turbulence. Nested grid AMR could avoid such a behavior, but abrupt changes in resolution can produce unphysical pressure jumps. The chosen geometry in our calculations, with an exponential growth of the grid cells outwards, naturally follow the scales of the problem, which smoothly grow outwards from the system.

We performed three additional 2D simulations to compare the influence of: geometry dimensionality, grid resolution, and size; model 2Dlf has the same domain size and resolution distribution as 3Dlf in the X and Y directions; model 2Dhf has the same domain size but twice the resolution of 2Dlf; and model 2Dhbf has an increased computational domain of $x \in [-100 a, 100 a]$ and $y \in [-100 a, 100 a]$ (central regions being $x \in [-2 a, 2 a]$ and $y \in [-2 a, 2 a]$), and a better effective resolution with a cell distribution: $N_x = [512, 512, 512]$ and $N_y = [512, 512, 512]$ cells (equivalent uniform resolution: 25600×25600). The model details are summarized in Tab. 1.

The pulsar-to-star wind momentum rate ratio, $\eta = \dot{P}_{\text{pw}}/\dot{P}_{\text{sw}}$, was fixed to 0.1 in 3D. To compare between the 3D and 2D results, we set $\eta_{2D} = \eta_{3D}^{1/2}$ to locate the two-wind contact discontinuity (CD) at the same distance from the pulsar (R_p), as

$$R_{p3D} = \eta_{3D}^{1/2} d / (1 + \eta_{3D}^{1/2}) \text{ vs } R_{p2D} = \eta_{2D} d / (1 + \eta_{2D}),$$

where d is the separation distance between the two stars. Under negligible pressure, the momentum rates are:

$$\dot{P}_{\text{pw}} \approx 4 \pi R_p^2 \Gamma^2 \beta^2 \rho_{\text{pw}} c^2 \text{ and } \dot{P}_{\text{sw}} \approx 4 \pi (d - R_p)^2 \rho_{\text{sw}} v_{\text{sw}}^2,$$

for the pulsar and the stellar winds, respectively; Γ , ρ_{pw} and β are the pulsar wind Lorentz factor, rest-frame density and c -normalized velocity, and ρ_{sw} and v_{sw} the stellar wind density and velocity. The pulsar spin-down luminosity can be approximated as

$$L_{\text{sd}} \approx (\Gamma - 1) \dot{P}_{\text{pw}} c / \beta.$$

A pulsar wind Lorentz factor $\Gamma = 2$ has been adopted because of resolution limitations, as the reconstruction of

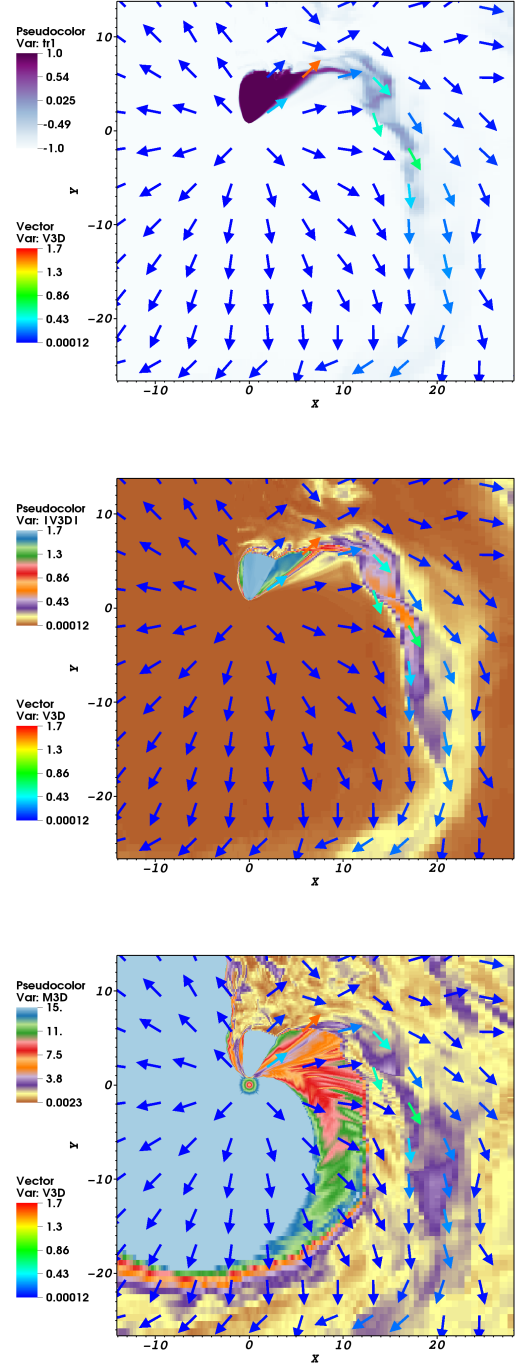


Fig. 5. Distribution of tracer, $\gamma\beta$, and Mach number (from top to bottom) for 3Dlf at $t = 5.2$ days.

the fluxes can lead to negative values in the term $(1 - \beta^2)$ if β is very close to 1. Our value of the Lorentz factor is the same as the one taken by Bosch-Ramon et al. (2012), and smaller than the conventional value $\Gamma \sim 10^4 - 10^6$ (see Khangulyan et al. 2012; Aharonian et al. 2012, and references therein), but still high enough to yield large wind density and velocity contrasts in the two-wind interaction region where instabilities trigger. In addition, given that for $\Gamma = 2$ the amount of kinetic energy is equal to the mass-rest energy of the pulsar wind, relativistic effects start to become apparent. A discussion of the instability development and the

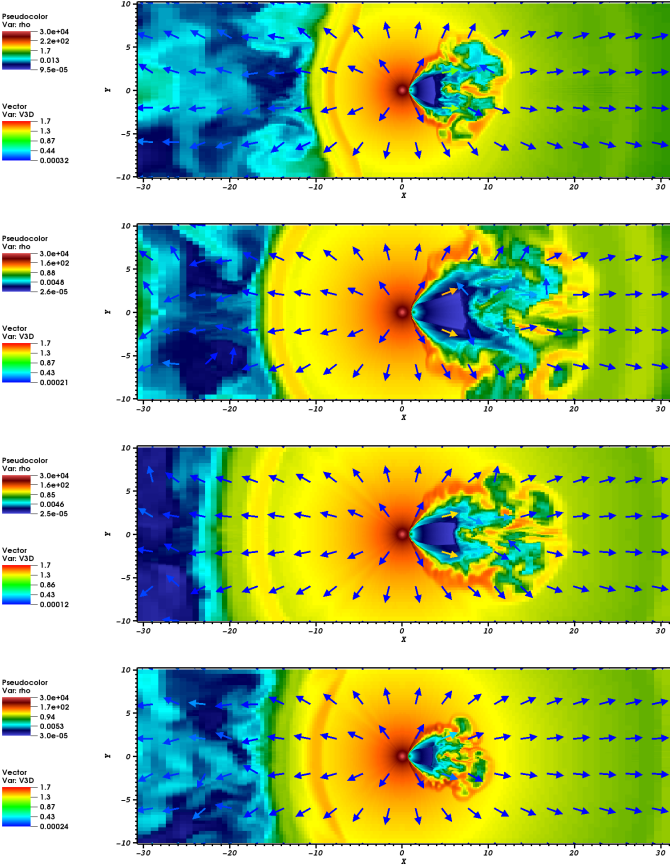


Fig. 6. Density distribution by colour, and arrows representing the flow motion direction, in the plane perpendicular to the orbit, and crossing the star-pulsar axis, for 3Dlf at: $t = 2.6, 3.9$ (apastron), $5.2, 5.85$ days (periastron) (from top to bottom).

relativistic effects in a simulation with a modest Lorentz factor is presented in Bosch-Ramon et al. (2012) (see also Lamberts et al. 2013). In short, on one hand, a high Lorentz factor implies a high wind density contrast favouring the instability growth in fluids; on the other hand, high Lorentz factors can slow down such a growth (e.g. Perucho et al. 2004; Bosch-Ramon et al. 2012). Therefore, the problem is numerically and physically complex, and specific thorough studies beyond the scope of this work are needed. The pressure in the pulsar wind at injection is negligible.

Unlike Bosch-Ramon et al. (2012), who simulated a generic case, in this work the orbital elements and stellar wind velocity (v_w) were taken similar to those of LS 5039 (Casares et al. 2005; Aragona et al. 2009; Sarty et al. 2011): eccentricity $e = 0.24$; period $T = 3.9$ days; orbital semi-major axis $a = 2.3 \times 10^{12}$ cm; and $v_w = 0.008c = 2.4 \times 10^8$ cm s $^{-1}$, with a stellar wind Mach number 7 at injection. Both the stellar and the pulsar winds were injected with spherical symmetry. For the given η , Γ and v_w values, the stellar and pulsar wind momentum rates, normalized to the stellar mass-loss rate, $\dot{M}_{-7} = (\dot{M}/10^{-7} M_\odot \text{ yr}^{-1})$, are $\dot{P}_{\text{sw}} \approx 6 \times 10^{27} \dot{M}_{-7}$ and $\dot{P}_{\text{pw}} \approx 6 \times 10^{26} \dot{M}_{-7} \text{ g cm s}^{-2}$ ($\approx 2 \times 10^{27} \dot{M}_{-7} \text{ g cm s}^{-2}$ in 2D), respectively. The corresponding spin down luminosity in 3D is $\approx 2 \times 10^{37} \dot{M}_{-7} \text{ erg s}^{-1}$. The values of v_w , Γ , \dot{M} , and η determine the wind den-

sities. The simulations do not include the magnetic field or anisotropy in the pulsar wind, although their impact should be small as long as the magnetic field for magnetic-energy to particle-energy density ratio (σ) is not too high (see Bogovalov et al. 2012, for an axisymmetric simulation of the present scenario adopting $\sigma \lesssim 1$).

The simulation starts running ($t = 0$) when the pulsar is at apastron: $(1.24a, 0, 0)$; to the right from the star: $(0, 0, 0)$; and the orbital motion, occurring in the XY -plane, is set counter-clockwise. Initially, the wind of the pulsar occupies a sphere of radius $a/2$, and a region bounded by a cone tangent to this sphere and oriented leftwards; the stellar wind occupies the rest of the grid. The initial setup is illustrated in Fig. 1. The injection region of the pulsar wind, which is injected continuously, is much smaller than the sphere of radius $a/2$. After starting the simulation, due to orbital motion the injector is relocated slowly enough to avoid numerical artifacts.

3. Results

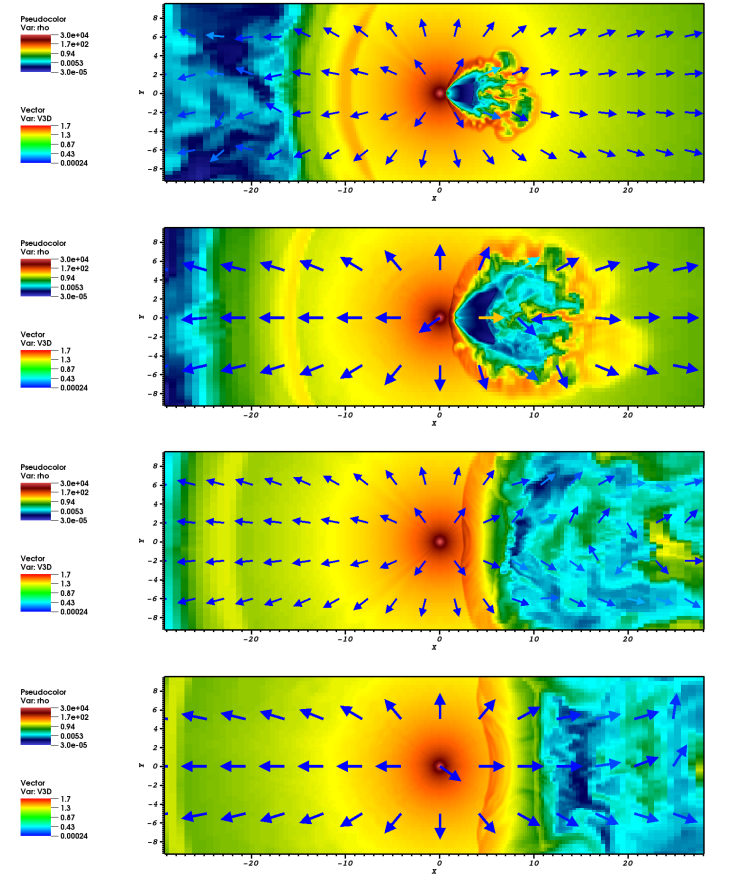


Fig. 7. Density distribution by colour, and arrows representing the flow motion direction, in a plane perpendicular to the orbit for 3Dlf at $t = 5.85$ days (periastron). The panels show different slices with an angle ϕ from the star-pulsar axis and clockwise: $\phi = 0, \pi/4, \pi/2, 3\pi/4$ (from top to bottom).

Figure 2 illustrates the 3D distribution of the density at apastron. The figure shows plane cuts in the XY -,

Table 1. Parameters of the models considered in this work. N_x , N_y and N_z are the resolution in the X -, Y - and Z -direction, respectively. The first number shows the resolution in the region with negative coordinates, the second one is the resolution in the uniform central region, and the third one is the resolution in the region with positive coordinates. X , Y and Z mark the boundaries between these three regions in each dimension; $v_{w,s} = v_{ws}/10^8 \text{ cm s}^{-1}$.

Name	N_x			N_y			N_z			X	Y	Z	$v_{w,s}$	η
3Dlf	s 128	u 256	s 128	s 128	u 256	s 128	s 64	u 128	s 64	-32,-2,2,32	-32,-2,2,32	-10,-1,1,10	2.4	0.1
2Dlf	s 128	u 256	s 128	s 128	u 256	s 128				-32,-2,2,32	-32,-2,2,32		2.4	0.3
2Dhf	s 256	u 512	s 256	s 256	u 512	s 256				-32,-2,2,32	-32,-2,2,32		2.4	0.3
2Dhbf	s 512	u 512	s 512	s 512	u 512	s 512				-100,-2,2,100	-100,-2,2,100		2.4	0.3

XZ - and YZ -planes taken after one full orbital period at $t = 3.9$ days. The structure has already reached a quasi-stationary state, which occurs after a simulation running time $\sim 1/6 - 1/8 \times T \sim 1/2$ days. Figure 3 shows the distribution of density in the orbital plane for 3Dlf at times $t = 2.6, 3.9$ (apastron), 5.2 and 5.85 days (periastron). For a better visualization of the results of 3Dlf, a zoom in of the density distribution around the pulsar during periastron is also shown in Fig. 4. Also, Fig. 5 shows the distribution of tracer (1 for the pulsar and -1 for the stellar wind, respectively), modulus of the four-velocity spatial component ($\gamma\beta$), and Mach number, for 3Dlf in the same plane. For completeness, Fig. 6 presents the density distribution for plane cuts along the star-pulsar axis and perpendicular to the orbital plane at the same times as those in Fig. 3. In addition, Figure 7 provides with the density distribution at periastron for plane cuts perpendicular to the orbital plane at different angles from the star-pulsar axis and clockwise: $\phi = 0, \pi/4, \pi/2, 3\pi/4$.

Figure 8 shows the distribution of density on the orbital plane for the same times as those in Fig. 3 for model 2Dlf. The same is shown in Fig. 9, but for a simulation with an increased resolution and grid size (2Dhbf), and slightly different orbital phases. Figure 10 shows the distribution of tracer, $\gamma\beta$, and Mach number, for 2Dhbf. Finally, Fig. 11 allows the comparison of the density distribution at the same orbital phase ($t = 5.85$ days) for the four simulations presented in this work (see Tab. 1)

3.1. 3D case

The quasi-stationary solution of the 3D simulation confirms what was already seen in 2D using planar coordinates in Bosch-Ramon et al. (2012). Despite some quantitative differences commented below, Figs. 2, 3, 4, and 5 display the same features as those found by Bosch-Ramon et al. (2012).

On one hand, the Kelvin-Helmholtz instability (KHI) starting at $\sim 2a$ from the pulsar quickly develops in the contact discontinuity, particularly in the leading edge of the two-wind interaction region. This instability, coupled to the orbital motion-induced Coriolis force, pushes material from the contact discontinuity (CD) to stop the propagation of the shocked pulsar wind coming from within the binary. This effect is apparent for instance in Fig. 4, at the leading edge of the shocked-wind structure, at the point where the CD widens due to the KHI instability. Since after termination within the binary the shocked pulsar wind reaccelerates becoming supersonic, a strong shock forms again when its path is blocked by the disrupted CD, heavily loaded with shocked stellar wind. The mass-load of the pulsar wind region is very apparent in the figures as abrupt and patchy

changes in density and tracer starting at $\sim 5 - 10a$ from the pulsar. This material from the CD penetrates further, stopping the unshocked pulsar wind with an almost perpendicular shock. Nevertheless, despite the apparent role of the KHI, we note that the Coriolis force is the main factor that shapes the interaction region, inducing the strong asymmetry of the interaction structure, as seen in Fig. 4. It is the very effect of the Coriolis effect that makes the shocked flow propagation outwards strongly non-ballistic, creating quasi-perpendicular shocks at the termination of the pulsar wind *behind* the pulsar (as seen from the star). These shocks are not of the same nature as the oblique shocks terminating the pulsar wind *behind* the pulsar found in axisymmetric, non-relativistic and relativistic, simulations of the same scenario but without orbital motion (e.g. Bogovalov et al. 2008; Lamberts et al. 2011). In particular, in axisymmetric cases the termination shock *behind* the pulsar disappears for $\eta \gtrsim 0.012$, and here $\eta = 0.1$. The *Coriolis shocks* found in our simulations are also different from those generated *behind* the pulsar when this is moving in the interstellar medium (e.g. Bucciantini et al. 2005), as the environment has a constant density. To finish with, as noted below, the size of the whole interaction structure clearly depends on the orbital phase, which would be difficult to explain if the *Coriolis shock* would not globally play a dominant dynamical role.

The orbital motion leads to a spiral-like structure, as expected. However, the coherence of this structure is strongly affected by the unstable nature of the flow, rich in strong shocks and mixing, induced by the Coriolis force, as predicted in Bosch-Ramon & Barkov (2011), and suggested by the numerical results of Bosch-Ramon et al. (2012). The present 3D results strengthen the thesis that the spiral shape is eventually lost, as the structure gets almost disrupted already within the grid, on scales $\sim 30a$. This is supported by Figs. 2–7, in which the lowest density regions of the *arm* of the spiral seem to split in different branches. The complexity of the matter distribution is best illustrated in the plane cuts perpendicular to the orbital plane in Figs. 2, 6 and 7, which also show how the pulsar wind is terminated at moderately different distances from the pulsar depending on latitude. This is explained by the different pressure found by the pulsar wind depending on the angle with which it faces the Coriolis force. The opening angle of the shocked two-wind structure is determined by the Coriolis force on the orbital plane, whereas in the perpendicular direction the opening angle is $\sim 60^\circ$, as in the case without orbital motion (e.g. Bogovalov et al. 2008). However, the KHI starting in the CD leads to fluctuations in the opening angle in this direction and, on larger scales, the shocked structure becomes wider, as the high

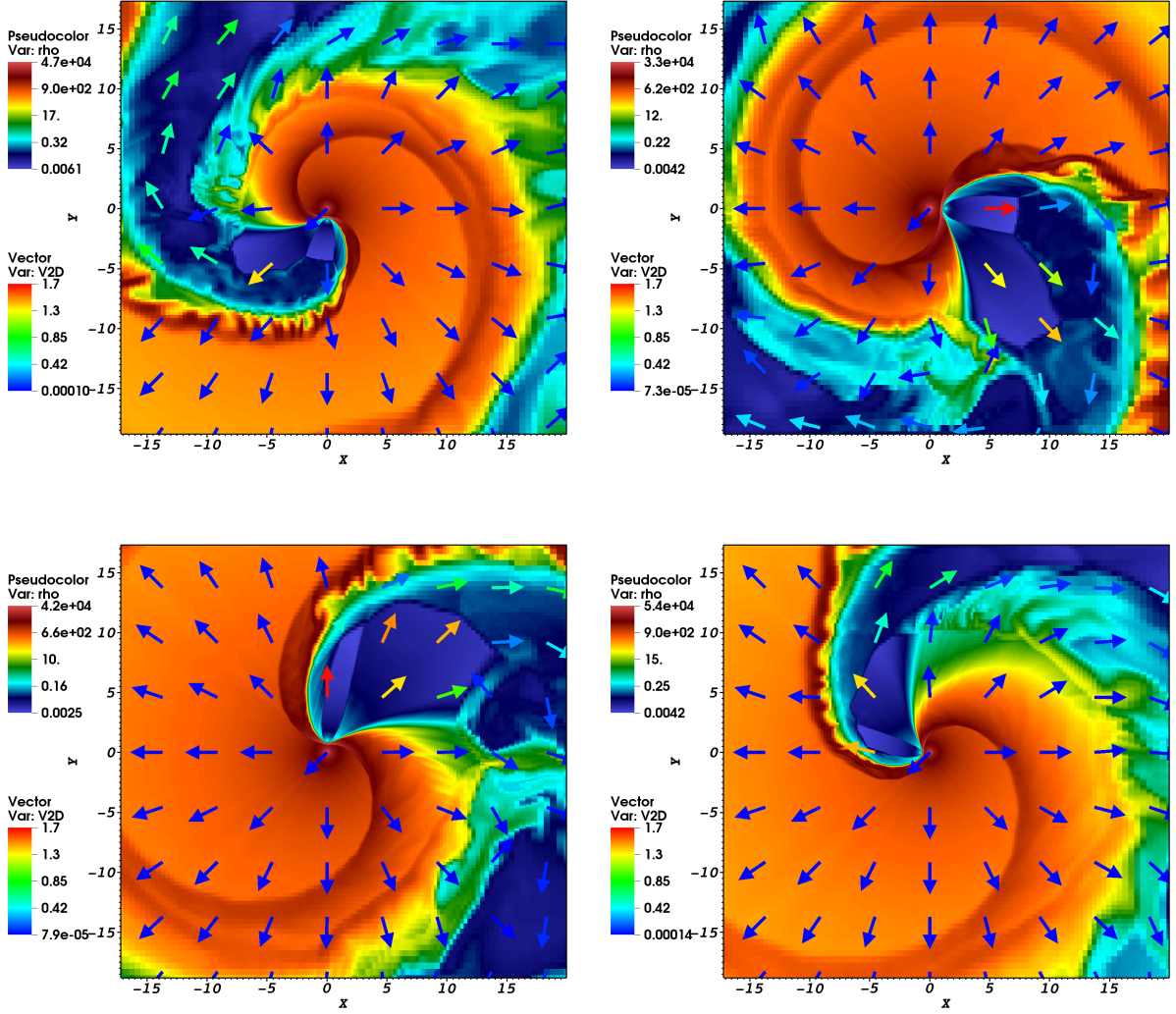


Fig. 8. Density distribution by colour, and arrows representing the flow motion direction, for 2Dlf at: $t = 2.6, 3.9$ (apastron), $5.2, 5.85$ days (periastron) (from top to bottom, and left to right).

sound speed of the shocked gas allows the latter to quickly transfer thrust to the vertical direction. As seen in the perpendicular cuts of Figs. 6 and 7, variations in d and in the pulsar angular velocity along the moderately eccentric orbit yield almost proportional variations in R_p and in the size of the whole interaction region. In particular, the ratio of d between apastron and periastron passages is ≈ 1.8 , whereas the whole interaction region size changes by a factor ≈ 1.6 in our simulations. Therefore, although size changes induced by instabilities are also taking place, as shown in Figs. 6 and 7, and also in 3, the region size evolves correlated with the orbital motion.

3.2. Comparison of 2D and 3D results

The results shown in Figs. 8 and 9 are very similar to those obtained by Bosch-Ramon et al. (2012) from 2D simulations with slightly different orbital parameters, and are also qualitatively very much alike to the 3D results just presented. As noted, the main features of the quasi-stationary solution in 2D and 3D are the same. The density distribution maps

of Figs. 8 and 3, and at the top panel of Fig. 11, allow for a comparison of results in 2D and 3D at periastron with the same resolution: the wind from the pulsar terminates closer to the latter but it is wider in 3D than in 2D; shocks, mixing, and turbulence start earlier, and mixing and turbulence are seemingly much stronger, in 3D. All this is also seen comparing Figs. 5 and 10.

The different η -values adopted in 3D and 2D, 0.1 versus $0.1^{1/2}$ (see Sect. 2), imply larger mass, momentum and energy fluxes for the pulsar wind in 2D, so it can explain why in 3D the termination of the pulsar wind and triggering of flow disruptive phenomena are closer to the pulsar. The higher strength of the disruptive phenomena in 3D would be on the other hand motivated by the higher number of geometric degrees of freedom. The wider opening angle of the unshocked pulsar wind region in 3D (see Fig. 11) would be explained by the stronger dilution of the shocked pulsar wind in the trailing edge of the interaction region.

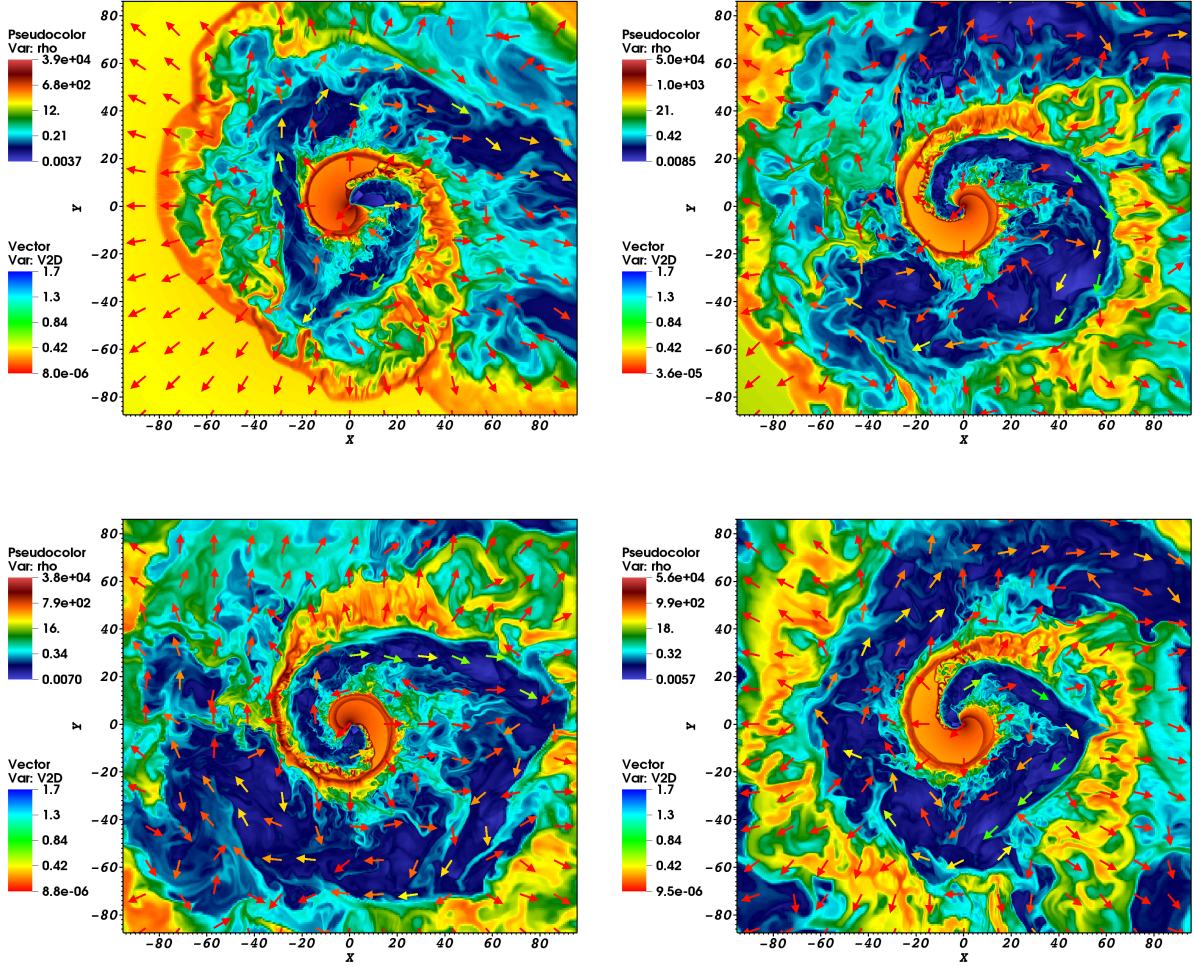


Fig. 9. Density distribution by colour, and arrows representing the flow motion direction, for 2Dhbf at: $t = 4.8, 6.3, 7.0$, and 9.85 days (\sim periastron) (from top to bottom, and left to right).

3.3. Effects of higher resolution

Figures 8, 9 and 11 (top right, and bottom left and right panels) allow for a comparison of the impact of increasing the resolution on the simulation results. Qualitatively, the higher resolution does not change significantly the flow structure and, as when comparing 3D and 2D simulations, the same major features are present in all the simulations: fast KHI growth in the CD, strong shocks terminating both the unshocked and the shocked pulsar wind, bending of the whole structure, development of turbulence, and strong two-wind mixing. However, with an increase in resolution, the KHI grows quicker, which leads to more turbulence downstream in the spiral, and also to pulsar wind termination closer to the pulsar as turbulent material from the CD exerts more pressure from one side (see Perucho et al. 2004, for a general study of the resolution influence on the evolution of KHI in numerical calculations). Given the higher dimensionality, a quicker instability development in 3D is expected, terminating the pulsar wind and generating turbulence even closer to the pulsar, if the resolution is increased. These statements will be tested in future work.

3.4. Effects of a larger grid

Figure 9 shows the density distribution evolution for the 2D simulation with the largest grid and the highest effective resolution. The maps show how the spiral starts disrupting through the growth of the KHI but also the Rayleigh-Taylor instability (RTI), which favors two-wind mixing and structure deformation. In addition, different spiral arms are connected through channels of higher density, while the spiral arms themselves seem to lose their integrity. This 2D simulation strongly suggests that in 3D the structure would lose coherence even closer ($< 100a$) from the binary, as predicted (Bosch-Ramon & Barkov 2011).

4. Discussion and summary

The results presented here indicate that the two-wind interaction structure is very unstable already on scales $\sim 10a$. In addition to structure bending, flow reacceleration, and full pulsar wind termination, features that are found in both 2D and 3D simulations, the KHI affecting the CD grows faster in 3D. This leads to turbulence and shocks further downstream the outflowing shocked winds, and also to efficient matter mixing that leads to more shocks, as dense

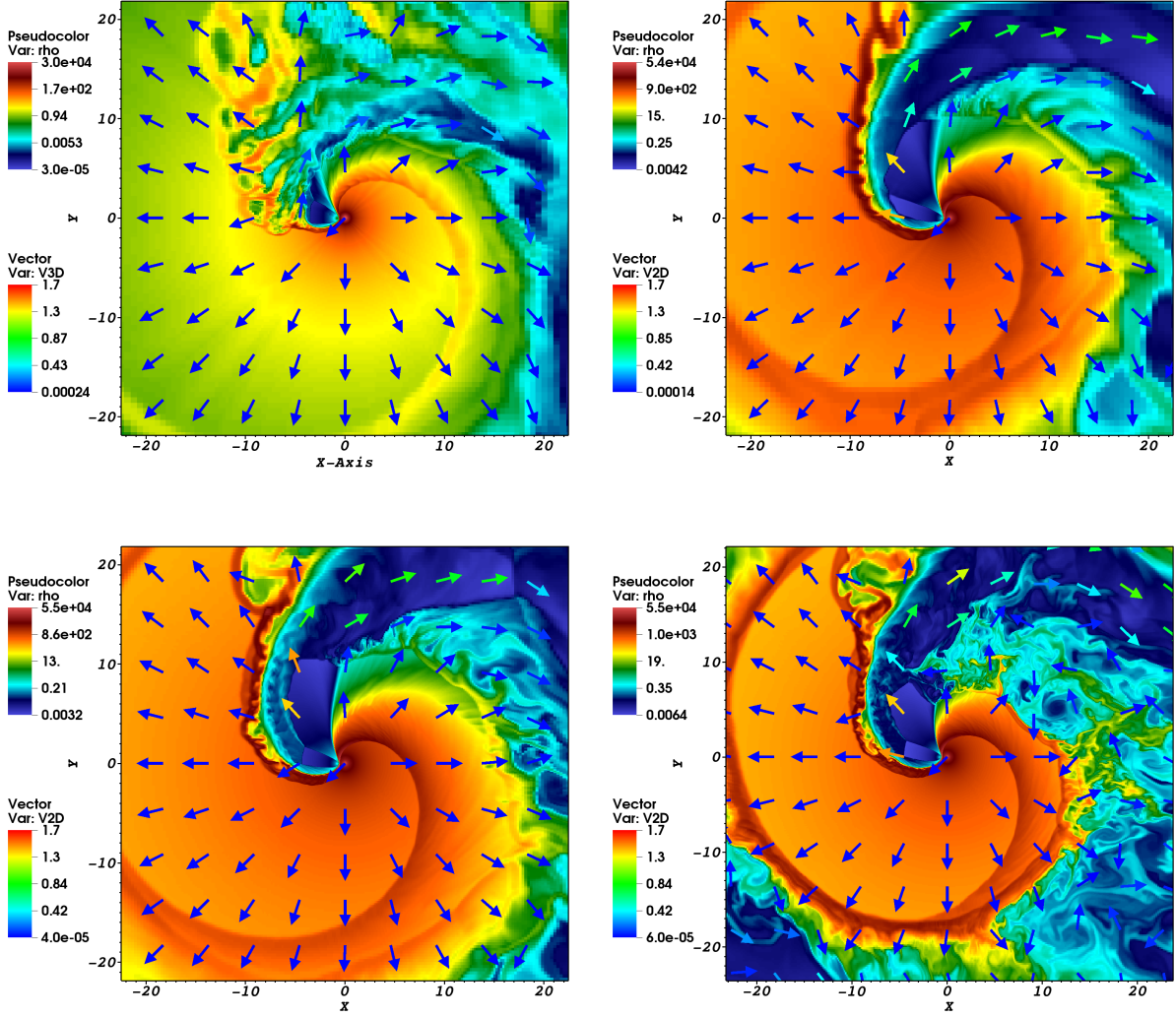


Fig. 11. Comparison of the density distribution (colour), and flow motion direction (arrows), in the orbital plane (XY) at $t = 5.85$ days (periastron) for 3Dlf, 2Dlf, 2Dhf, and 2Dhbf (from top to bottom, and left to right).

clumps of stellar material penetrate into the region occupied by the fast and light shocked pulsar wind. All this was already found in previous 2D simulations (Bosch-Ramon et al. 2012), but in 3D all these processes occur closer to the binary. An enhancement of the resolution will make the interaction region more unsteady, likely shortening further the distances on which the KHI develops, and enhancing even more two-wind mixing. It is interesting to note that the bending length in 3D is ~ 3 times farther than the point of balance between the Coriolis force and the pulsar wind (see Eq. 9 in Bosch-Ramon & Barkov 2011). This is expected, as the wave triggered by pressure balance takes time to transfer energy and momentum to the whole shocked flow structure. Although our 3D simulations are capturing some relevant features of the shocked two-wind structure, a natural future step should be to increase the grid resolution. For instance, to increase the Lorentz factor of pulsar wind by a factor of a few, the resolution of the central part of the computational domain should be doubled. In addition, as indicated by the 2D simulations (see Fig. 11), the large scale turbulence would be well resolved with 3-4 times more resolution in the grid periphery than in our current 3D

setup. Such an increase in resolution would require about 10^7 cpu hours. This is a demanding calculation, but we will carry it out as it is a necessary step in the project.

On larger scales, $\sim 10 - 100 a$, the radial pressure exerted by the shock mixed flow outwards triggers strong RTI, which are already hinted in 3Dlf but are seen strongly developed in 2Dhbf, to the extent of disrupting and mixing the arms of the spiral formed by the orbital motion. This environment, still relatively close to the star to have enough radiation targets, but large enough as well to be resolved in radio, is very rich in candidate sites for non-thermal emission (see the discussion in Bosch-Ramon et al. 2012) for which Doppler boosting can be an issue given the non-uniform velocity distribution. In particular, as seen for instance in Figs. 3 and 9, shocked pulsar wind material is found to move straight along quite large distances ($\sim 10 a$). Being shocked, with a likely content of non-thermal particles, being relatively close to the star, and moving with at least mildly relativistic velocities (Lorentz factor γ), emission Doppler boosted by a factor of $\sim 16\gamma^2 \gtrsim 10$ would be seen by the observer viewing this flow with an angle $< 1/\gamma$ from its axis. For large systems such as PSR B1259-63,

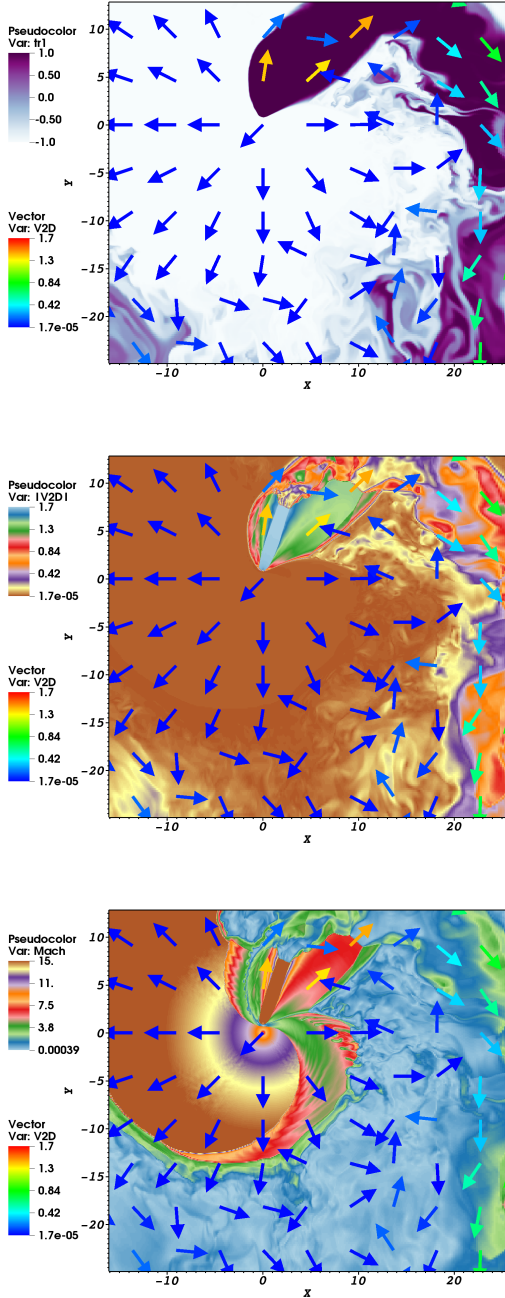


Fig. 10. Distribution of tracer, $\gamma\beta$, and Mach number (from top to bottom) for 2Dhbf at $t = 5.2$ days.

X-rays could be also useful to observationally probe the shocked flow structure on scales $\sim 10^{17}$ cm (Kargaltsev et al. 2014), and even further away (Durant et al. 2011), on scales similar to those of the shocked wind-fed bubble (Bosch-Ramon & Barkov 2011).

It is noteworthy that, due to momentum and energy isotropization, the evolution of the shocked flow structure in the perpendicular direction gets broader further downstream than in the case without orbital motion. The study of this process deserves specific simulations with a larger grid in the Z -direction. In the same line, a more accurate characterization of the evolution of the interaction structure along the orbit would deserve higher resolution, and

eventually a larger grid size. However, this is computationally very costly. Thermal cooling should be also included as the shock of the stellar wind may be radiative, making the collision region more unstable and favouring mixing of the CD and its disruption (Pittard 2009). This would increase even further turbulence and the presence of shocks in the shocked pulsar wind region. More feasible, but requiring the simplification of the region containing the system, is the simulation of the shocked flow structure with the environment on large scales, which was predicted to take place as a fast dense non-relativistic wind colliding with the surrounding medium (Bosch-Ramon & Barkov 2011). Other line of research remaining open is the computation of the emission from the shocked flows using the hydrodynamical information, which first could be carried out in the test-particle approximation. Another improvement should be carrying relativistic simulations with an anisotropic and/or inhomogeneous stellar wind³, e.g. adding an equatorial disc, as several of the known gamma-ray binaries host Be stars. Finally, VLBI radio data are very important to observationally characterize the shocked flow structure on the simulated scales (e.g. Moldón et al. 2011b,a, 2012).

Acknowledgements. The calculations were carried out in the CFCA cluster of National Astronomical Observatory of Japan. We thank Andrea Mignone and the *PLUTO* team for the possibility to use the *PLUTO* code. We especially thanks to Claudio Zanni for technical support. The visualization of the results was done using the VisIt package. The research leading to these results has received funding from V.B.-R. acknowledge support by the Spanish Ministerio de Economía y Competitividad (MINECO) under grants AYA2013-47447-C3-1-P. This research has been supported by the Marie Curie Career Integration Grant 321520. BMV acknowledge partial support by JSPS (Japan Society for the Promotion of Science): No.2503786, 25610056, 26287056, 26800159. BMV also MEXT (Ministry of Education, Culture, Sports, Science and Technology): No.26105521 and RFBR grant 12-02-01336-a. V.B.-R. also acknowledges financial support from MINECO and European Social Funds through a Ramón y Cajal fellowship.

References

- Abdo, A. A., Ackermann, M., Ajello, M., et al. 2011, *ApJ*, 736, L11
- Aharonian, F., Akhperjanian, A. G., Aye, K.-M., et al. 2005, *A&A*, 442, 1
- Aharonian, F. A., Bogovalov, S. V., & Khangulyan, D. 2012, *Nature*, 482, 507
- Aragona, C., McSwain, M. V., Grundstrom, E. D., et al. 2009, *ApJ*, 698, 514
- Barkov, M. V. & Khangulyan, D. V. 2012, *MNRAS*, 2375
- Bogovalov, S. V., Khangulyan, D., Koldoba, A. V., Ustyugova, G. V., & Aharonian, F. A. 2012, *MNRAS*, 419, 3426
- Bogovalov, S. V., Khangulyan, D. V., Koldoba, A. V., Ustyugova, G. V., & Aharonian, F. A. 2008, *MNRAS*, 387, 63
- Bosch-Ramon, V. & Barkov, M. V. 2011, *A&A*, 535, A20
- Bosch-Ramon, V., Barkov, M. V., Khangulyan, D., & Perucho, M. 2012, *A&A*, 544, A59
- Bucciantini, N., Amato, E., & Del Zanna, L. 2005, *A&A*, 434, 189
- Casares, J., Ribó, M., Ribas, I., et al. 2005, *MNRAS*, 364, 899
- Chernyakova, M., Abdo, A. A., Neronov, A., et al. 2014, *MNRAS*, 439, 432
- Colella, P. & Woodward, P. R. 1984, *Journal of Computational Physics*, 54, 174
- Dubus, G. 2013, *A&A Rev.*, 21, 64
- Durant, M., Kargaltsev, O., Pavlov, G. G., Chang, C., & Garmire, G. P. 2011, *ApJ*, 735, 58

³ Regarding anisotropic and/or inhomogeneous stellar winds, see Paredes-Fortuny et al. (2014) for the axisymmetric case, and Okazaki et al. (2011); Takata et al. (2012) for the non-relativistic case.

- Johnston, S., Manchester, R. N., Lyne, A. G., et al. 1992, *ApJ*, 387, L37
- Kargaltsev, O., Pavlov, G. G., Durant, M., Volkov, I., & Hare, J. 2014, *ApJ*, 784, 124
- Khangulyan, D., Aharonian, F. A., Bogovalov, S. V., & Ribo, M. 2012, *ApJ*, in press
- Lamberts, A., Dubus, G., Fromang, S., & Lesur, G. 2012a, in *American Institute of Physics Conference Series*, Vol. 1505, American Institute of Physics Conference Series, ed. F. A. Aharonian, W. Hofmann, & F. M. Rieger, 406–409
- Lamberts, A., Dubus, G., Lesur, G., & Fromang, S. 2012b, *A&A*, 546, A60
- Lamberts, A., Fromang, S., & Dubus, G. 2011, *MNRAS*, 418, 2618
- Lamberts, A., Fromang, S., Dubus, G., & Teyssier, R. 2013, *A&A*, 560, A79
- Maraschi, L. & Treves, A. 1981, *MNRAS*, 194, 1P
- Mignone, A. & Bodo, G. 2005, *MNRAS*, 364, 126
- Mignone, A., Bodo, G., Massaglia, S., et al. 2007, *ApJS*, 170, 228
- Moldón, J., Johnston, S., Ribó, M., Paredes, J. M., & Deller, A. T. 2011a, *ApJ*, 732, L10
- Moldón, J., Ribó, M., & Paredes, J. M. 2011b, *A&A*, 533, L7
- . 2012, *A&A*, 548, A103
- Negueruela, I., Ribó, M., Herrero, A., et al. 2011, *ApJ*, 732, L11
- Okazaki, A. T., Nagataki, S., Naito, T., et al. 2011, *PASJ*, 63, 893
- Paredes, J. M., Bednarek, W., Bordas, P., et al. 2013, *Astroparticle Physics*, 43, 301
- Paredes-Fortuny, X., Bosch-Ramon, V., Perucho, M., & Ribó, M. 2014, *A&A*, 0
- Perucho, M., Hanasz, M., Martí, J. M., & Sol, H. 2004, *A&A*, 427, 415
- Pittard, J. M. 2009, *MNRAS*, 396, 1743
- Portegies Zwart, S. F. & Yungelson, L. R. 1999, *MNRAS*, 309, 26
- Romero, G. E., Okazaki, A. T., Orellana, M., & Owocki, S. P. 2007, *A&A*, 474, 15
- Sarty, G. E., Szalai, T., Kiss, L. L., et al. 2011, *MNRAS*, 411, 1293
- Takata, J., Okazaki, A. T., Nagataki, S., et al. 2012, *ApJ*, 750, 70
- Tam, P. H. T., Huang, R. H. H., Takata, J., et al. 2011, *ApJ*, 736, L10